In Vitro Study of α-Synuclein Protofibrils by Cryo-EM Suggests a Cu^{2+}-Dependent Aggregation Pathway

Hangyu Zhang,[†] Amy Griggs,[‡] Jean-Christophe Rochet,[‡] and Lia A. Stanciu[†§*]
[†]Weldon School of Biomedical Engineering, [‡]Department of Medicinal Chemistry and Molecular Pharmacology, and [§]School of Materials Engineering, Purdue University, West Lafayette, Indiana

ABSTRACT The aggregation of α-synuclein is thought to play a role in the death of dopamine neurons in Parkinson's disease (PD). Alpha-synuclein transitions itself through an aggregation pathway consisting of pathogenic species referred to as protofibrils (or oligomer), which ultimately convert to mature fibrils. The structural heterogeneity and instability of protofibrils has significantly impeded advance related to the understanding of their structural characteristics and the amyloid aggregation mystery. Here, we report, to our knowledge for the first time, on α-synuclein protofibril structural characteristics with cryo-electron microscopy. Statistical analysis of annular protofibrils revealed a constant wall thickness as a common feature. The visualization of the assembly steps enabled us to propose a novel, to our knowledge, mechanisms for α-synuclein aggregation involving ring-opening and protofibril-protofibril interaction events. The ion channel-like protofibrils and their membrane permeability have also been found in other amyloid diseases, suggesting a common molecular mechanism of pathological aggregation. Our direct visualization of the aggregation pathway of α-synuclein opens up fresh opportunities to advance the understanding of protein aggregation mechanisms relevant to many amyloid diseases. In turn, this information would enable the development of additional therapeutic strategies aimed at suppressing toxic protofibrils of amyloid proteins involved in neurological disorders.

INTRODUCTION

Parkinson's disease (PD) affects 1–2% of people over the age of 60 with a drastic increase of the prevalence of PD in the following decades (1,2). The aggregation of α-synuclein is increasingly believed to play a critical part in the etiology of PD (3–5). Importantly, the abnormal protein aggregation characterizes a considerable number of human diseases, such as Alzheimer's, Parkinson's, and Huntington's diseases, and type II diabetes (4,6,7). Moreover, the self-assembly of polypeptides to form amyloid structures is a common phenomenon that was also found in the peptides and proteins not related to any amyloid diseases (8–11). Therefore, information on the α-synuclein aggregation mechanism would be valuable not only for the understanding of PD pathogenesis and the development of additional therapeutic strategies, but also for related researches of other amyloid diseases and the exploration of self-assembly phenomena.

Accumulating evidence implies that protofibrils, rather than mature fibrillar aggregates, may be the pathogenic species (12–14). Various forms of α-synuclein protofibrils including spherical, annular, and chain-like aggregations have been reported, showing the heterogeneity of protofibrils (14–16). Among these protofibril structures, the annular protofibrils aroused great interest. In early in vitro studies, the annular protofibrils could be formed after prolong incubation from heterogeneous spherical protofibrils with an average height of 2.7 nm, and be observed in membrane-associated form (16). PD-linked mutants were found to promote annular protofibril formation, suggesting a pore-like mechanism for the toxicity of β-sheet rich annular protofibrils (16,17). Besides PD (17–19), ion channel-like annular protofibrils have also been found in other amyloid diseases, such as Alzheimer's disease (18–21), prion-related diseases (22), and type II diabetes (23), suggesting a common molecular mechanism of aggregation (24,25). However, details of the protofibril structures and aggregation pathway of α-synuclein remain poorly understood due to the structural heterogeneity and instability of protofibrils (7). From the literature, it is difficult to determine whether annular protofibrils are on the direct pathway to mature fibrils and to understand how they finally convert to fibrils. In addition, with traditional visualization methods such as AFM and negative stain transmission electron microscopy (TEM), the structures and sizes of protofibrils observed were altered from their native state. For instance, the correlation of annular protofibrils and tubular protofibrils was blurred in negative stain TEM images (17).

The wall thicknesses of annular protofibrils were also much larger than those calculated with molecular dynamics simulations (25,26). To characterize the structure of α-synuclein protofibrils and unravel the aggregation mystery, we used cryo-electron microscopy (cryo-EM) for the first time, to our knowledge, to study protofibrils in solutions. Upon the measurement of the true size of annular protofibrils and the visualization of aggregation steps, we found the correlation of annular protofibrils and fibrils, and further proposed an aggregation pathway.

Submitted January 9, 2013, and accepted for publication April 23, 2013.

*Correspondence: lstanciu@purdue.edu

Editor: Elizabeth Rhoades.

0006-3495/13/06/2706/8 $2.00

http://dx.doi.org/10.1016/j.bpj.2013.04.050

MATERIALS AND METHODS

Protein expression and purification

Cells of the *E. coli* strain BL21 (DE3) were transformed with the plasmid pT7-7 wild-type (WT) α-synuclein incubated at 37°C in the presence of 1 mM isopropyl β-D-thiogalactopyranoside to induce protein expression. The cells were harvested by centrifugation and resuspended in buffer (10 mM Tris-HCl, pH 8.0, 1 mM EDTA, 1 mM PMSF). The cell suspension was frozen, thawed, and then lysed with a French pressure cell (psi > 1000) (Thermo Electron, Waltham, MA). Partial purification of the α-synuclein lysate was achieved by two successive ammonium sulfate precipitations (30 and 50% saturation) at 4°C. The pellet was resuspended in 10 mM Tris-HCl, pH 7.4 and boiled for 5 min. Centrifugation was performed to remove insoluble proteins, and the supernatant was passed through a 0.22-μm filter and applied to a DEAE Sepharose FF column (16 × 100 mm, Amersham Biosciences, Sunnyvale, CA). Alpha-synuclein was eluted from the column with an increasing concentration gradient of NaCl. Fractions containing α-synuclein were identified by sodium dodecyl-sulfate polyacrylamide gel electrophoresis with Coomassie-Blue staining and pooled, and the resulting protein solution was dialyzed against 10 mM NH_4HCO_3 for 24 h and lyophilized. The protein was ~95% pure.

Fibrillization

WT α-synuclein was reconstituted in 1 × phosphate-buffered saline (PBS), 0.02% (w/v) NaN_3 and then passed through a 0.22 μm and 100 kDa molecular-weight cut-off (MWCO) filter. The remaining protein was then dialyzed in the same buffer for 24 h at 4°C. WT α-synuclein (400 μM) was incubated in the absence and presence of 40 μM copper sulfate (40 μM) at 37°C on a rolling rack. Aliquots were collected at different time points and stored at −80°C.

Fourier transform infrared spectroscopy

Attenuated total reflectance (ATR)-Fourier transform infrared (FTIR) spectroscopy data were recorded on a Spectrum 100 FTIR spectrometer equipped with a universal ATR sampling accessory (Perkin Elmer, Waltham, MA). WT α-synuclein solution in the presence of copper sulfate at the incubation time of 60 h was first centrifuged for 5 min at 16,000 RCF and filtered through a 200-μm filter to eliminate insoluble aggregates. Then the filtrates were loaded into Ultra-0.5 centrifugal filter devices (MWCO 100 kDa; Amicon, Danvers, MA) to separate the particles based on the molecular weight. The separated protein solution was spread out and dried to form a thin film on a Diamond/ZnSe crystal (27,28). Spectrum data were analyzed with the ORIGINPRO software from OriginLab (Northampton, MA). Curve-fitting function was used to estimate secondary structure components and corresponding percentages according to the peak positions identified by second derivatives and Fourier self-deconvolution (27–29).

Thioflavin T fluorescence

Aliquots (100 μL) of WT α-synuclein (400 μM) and Thioflavin T (ThT) (100 μM) in the absence and presence of copper sulfate (40 μM) in 1 × PBS, pH7.4, 0.02% NaN_3 were pipetted into a 96-well plate. The aggregation was monitored at 37°C using a Gemini EM Fluorescence Microplate Reader (Molecular Devices, Sunnyvale, CA) with an excitation wavelength of 440 nm and an emission wavelength of 482 nm. The fluorescence was measured every 15 min after the 30-s shaking.

Transmission electron microscopy image collection

Cryo-EM specimens were prepared on holey carbon C-flat 2/2 grids (Protochips, Raleigh, NC) using a Cp3 cryo-plunger (Gatan, Pleasanton, CA). For cryo-negative staining (cryo-NS) test, the grids with samples were stained by layering on 100 μL aliquots of saturated ammonium molybdate (pH 7.2) for 1 min, before the grids were blotted (30,31). Negative stain specimens were applied to glow-discharged, carbon-coated copper grids. Then grids were rinsed with three drops of PBS and stained by a drop of 1% uranyl acetate. Images were collected on SO-163 films (Kodak, Rochester, NY) or 4 K charge-coupled device (Gatan) with a CM200 TEM operating at 200 kV (Philips, Amsterdam, Netherlands).

Image processing

The EMAN2 software package (National Center for Macromolecular Imaging, Houston, TX) was used to box particles and generate reference-free class averages. Due to the structural heterogeneity, the particles could not be automatically boxed or classified correctly. Therefore, only one class of particles was boxed manually each time, and this class was then used to generate a class average with EMAN2. Annular protofibrils were classified into four groups based on their outer diameters. Sixty particles from class E, F, and G were randomly selected for diameter measurement, whereas 20 particles were chosen from class H (only 28 particles in all). The wall thickness (L) was calculated from $L = 1/2 \times (D_o - D_i)$ where D_o and D_i were the outer and inner diameter pair of each individual ring. In general, the diameters that provided the smallest wall thickness were measured to minimize the projection angle problem. Moreover, the rings were actually imperfect polygons, so the vertices were avoided when measuring the diameters.

RESULTS AND DISCUSSION

Structural features of protofibrils

Cryo-EM was used to monitor the aggregation process and collect protofibril images at various incubation times. All cryo-EM images of protofibrils presented here were collected in presence of Cu^{2+} at $t = 60$ h unless otherwise specified. Copper (II) cation (40 μM) was added into solutions of wild-type (WT) α-synuclein (400 μM) to accelerate the aggregation and provide sufficient protofibrils for cryo-EM testing. There were essentially no differences in protofibril structures from 48 h to 60 h incubation time. However, the aggregation rate varied from batch to batch. Various structures of protofibrils (including spherical and annular) and α-synuclein aggregates of different sizes were observed, which was in agreement with previous reports (Fig. 1, *A* and *B*) (16–18). Generally, the protofibrils could be roughly sorted into two types, based on their shapes and brightness of corresponding cryo-EM images: annular protofibrils with very low brightness (Fig. 1 *A*), and α-synuclein aggregates that were brighter (Fig. 1 *B*). In the annular protofibril images, a large number of particles did not show the central hole, as a result of different projection angles.

Single particle averaging was applied to analyze the protofibril structures from cryo-EM images. The reference-free class average program in the EMAN2 software package is generally used to classify different views of homogenous particles. Although we cannot aim to reach similar results with heterogeneous α-synuclein protofibrils, the program can still extract their common structural features. A class of spherical protofibrils with a diameter of ~3 nm was

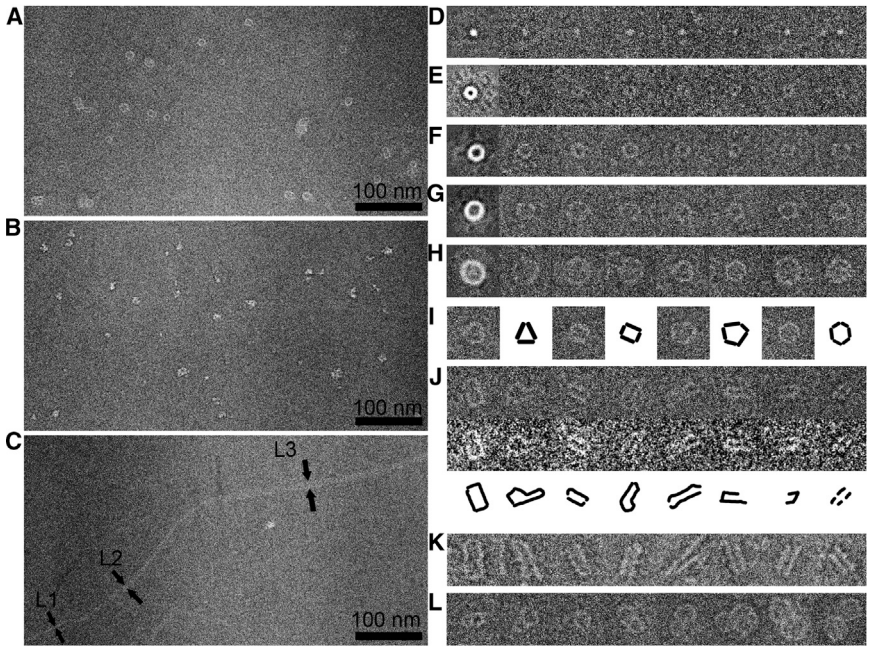

FIGURE 1 Cryo-EM images of heterogeneous structures of WT α-synuclein. (*A* and *B*) Representative images of annular protofibrils and α-synuclein aggregates, respectively. (*C*) Image showing nontwist fibrils with three different widths ($L1 \approx 2.5$ nm, $L2 \approx 5.4$ nm, and $L3 \approx 12$ nm). (*D–H*) Images showing different classes of protofibrils. The first image of each row represents a class average calculated from 25 particles (*D*), 135 particles (*E*), 112 particles (*F*), 143 particles (*G*), and 28 particles (*H*). Each class average image is followed by seven images consisting of representative particles from the same class. (*I*) Images of typical annular protofibrils demonstrating polygon structures, together with corresponding cartoons emphasizing the polygon features. (*J*) Images of particles in the ring opening step, shown before (*top row*) or after (*middle row*) applying a low-pass filter; (*bottom row*) corresponding cartoons for visualization assistance. (*K*) cryo-NS images showing the ring opening step. (*L*) Images of laterally aggregated annular protofibrils. The size of each square box in panels *D–L* is 30.5 nm.

selected from α-synuclein aggregate images (Fig. 1 *D*). Their size was comparable to the structure reported as being able to convert to annular protofibrils after prolonged incubation (16). Four classes of particles were selected from annular aggregate images (Fig. 1, *E–H*). In Fig. 1, *D–H*, class averages are exhibited in the first images of each row, followed by seven representative particles of corresponding classes. The molecular weights of annular protofibrils are close to the imaging resolution limit of cryo-EM (17), making their low dose cryo-EM images rather noisy; nevertheless, their shape is still discernible. The generation of clear class averages supported the existence of these small protofibrils, and this was also confirmed via negative stain images (see Fig. S1 in the Supporting Material). The significant improvement of contrast in class average images implied the structural similarity of protofibrils within each class.

Statistical analysis of annular protofibrils revealed that they had identical wall thickness regardless of their respective diameters. We classified the annular protofibrils into four groups, based on their outer diameters. From the class average images we found that the wall thicknesses of the rings (set as L) were similar among the four groups. To confirm this result, the outer and inner diameters (set as D_o and D_i, respectively) of the annular protofibrils in each class were measured and shown in Fig. 2. L calculated from D_o and D_i was constant (~2.4 nm) regardless of the ring diameter. At close inspection, it was revealed that most of the annular protofibrils actually were not annuli, but imperfect polygons possessing variable amounts of straight-protofilament-like subunits. This observation was in agreement with other reports using AFM or molecular dynamics simulations as the main investigative methods (25,26,32). Four typical annular protofibrils with this feature are shown in Fig. 1 *I*. Furthermore, ATR-FTIR analysis was applied to investigate the secondary structure of protofibrils formed during the incubation. The spectra were decomposed, in terms of the peak positions obtained from second derivatives and Fourier self-deconvolution, by fitting with Gaussian curves. The protein sample in presence of Cu^{2+} at the incubation time of 60 h was separated by centrifugal filters (MWCO 100 kDa). The particles larger than 100 kDa displayed widely distributed annular structures in the negative stain TEM image (Fig. 3 *D*) and high β-sheet

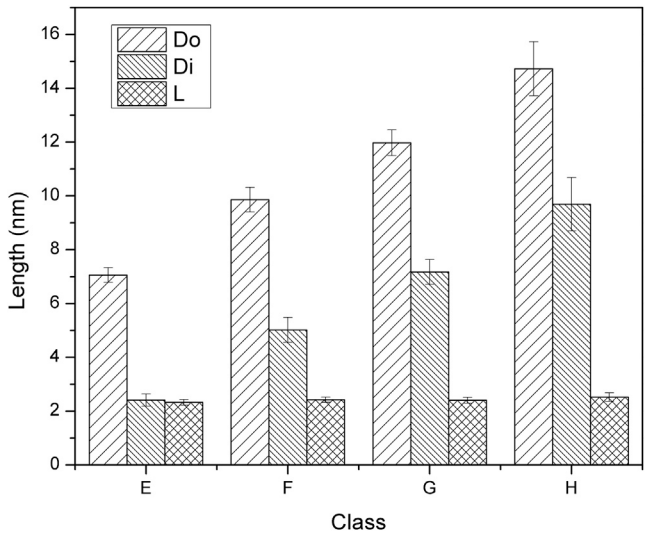

FIGURE 2 Statistical analysis of the outer diameter (D_o), inner diameter (D_i) and wall thickness ($L = 1/2 \times (D_o - D_i)$) of each class of annular protofibrils (mean $\pm$ SD, $n = 60$ in classes E, F, and G; $n = 20$ in class H). The wall thicknesses (L) of classes E, F, G, and H are 2.32 $\pm$ 0.10 nm, 2.42 $\pm$ 0.09 nm, 2.40 $\pm$ 0.11 nm, and 2.52 $\pm$ 0.16 nm, respectively.

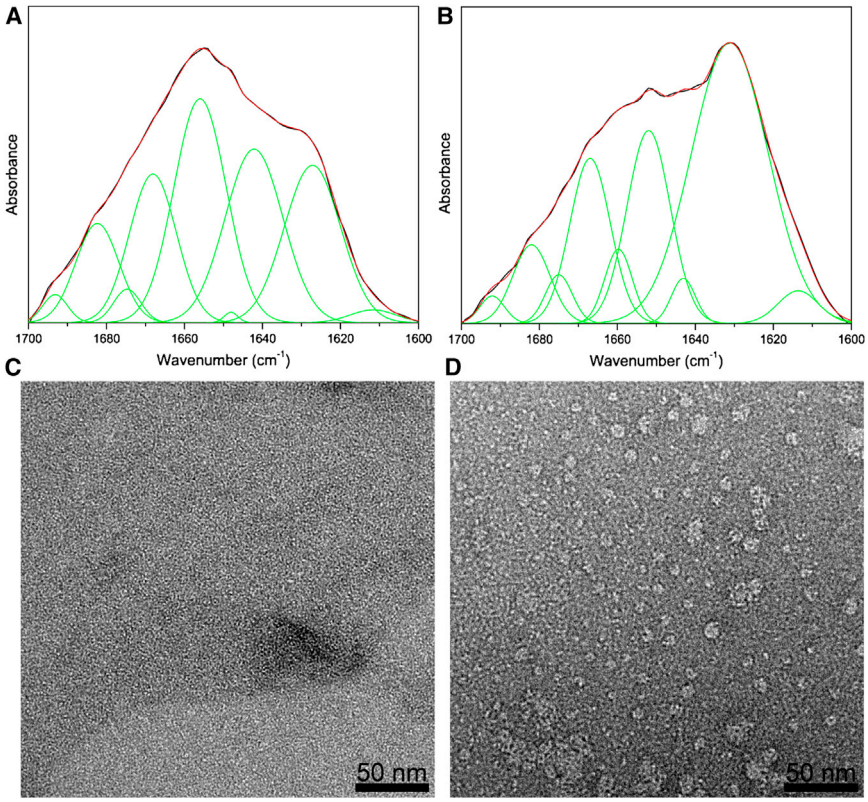

FIGURE 3 The analysis of the secondary structure of annular protofibrils. ATR-FTIR spectra of α-synuclein samples in the fraction of particles smaller than 100 kDa (*A*) and the fraction of particles larger than 100 kDa (*B*). The experimental FTIR spectra (*black*) were decomposed by fitting with Gaussian curves (*green*). The cumulative fit curve was shown (*red*). Negative stain TEM images of particles smaller than 100 kDa (*C*) and particles larger than 100 kDa (*D*).

contribution (49.8%) with the peaks at approximately at 1631 cm^{-1} and 1692 cm^{-1} in the FTIR spectrum (Fig. 3 *B*). On the other hand, no annular structures were observed in the particles smaller than 100 kDa (Fig. 3 *C*), which exhibited much lower β-sheet content (22%) with the peaks at ~1627 cm^{-1} and 1693 cm^{-1} (Fig. 3 *A*).

The existence of a large amount of annular protofibrils coinciding with high β-sheet content suggested that annular protofibrils were β-sheet-rich structures, which is in agreement with previous reports. Diversified β-sheet-rich amyloid protofibrils were reported to transiently form earlier than fibrils and then disappeared along with fibril formation (24,33–35). Particularly, the annular protofibrils of the PD linked mutant A53T and Aβ were found to exhibit high β-sheet content (17,19). The observation of rigid straight-protofilament-like subunits in this research also supported that the annular protofibrils were in a β-sheet conformation. Consequently, we inferred that annular protofibrils of different diameters appeared to be constructed of small and nontwisted filamentous structure of ≈2.4 nm width that might be equivalent to the protofilament in a mature fibril (see below).

Annular protofibrils and fibrils

Coincidentally, the width of the thinnest fibril (*L*1) in Fig. 1 *C* was ~2.5 nm, close to the wall thickness of the annular protofibrils. The widths of the other two thicker fibrils in Fig. 1 *C* were *L*2 ≈ 5.4 nm and *L*3 ≈ 12 nm. One report that used cryo-NS TEM to image α-synuclein structures showed that nontwist fibrils of α-synuclein exhibited a width of 13 ± 1 nm and comprised two filaments of ≈5.5 nm width, each of which was composed of two protofilaments with a width of ≈2.0 nm (36). The characteristics of the three types of fibrils in Fig. 1 *C* showed similar results. The small differences between our measured values and previous data might result from variations of the projection angles and measurement errors. Accordingly, the three types of fibrils with widths of *L*1, *L*2, and *L*3 in Fig. 1 *C* could be attributed to the protofilament, the filament, and the mature fibril, respectively.

The aggregation pathway

At the early stage of the aggregation, no fibrils or identifiable protofibrils were observed (Fig. 4, *A* and *B*), showing that only monomers, dimers, or small oligomers, which were too small to be observed by cryo-EM, existed in the system. Annular protofibrils were first found at 48 h incubation time (Fig. 4 *C*) and were still the dominant species at $t = 56$ h in cryo-EM images (Fig. 4 *D*). Both annular protofibrils and fibrils could be easily found at $t = 60$ h (Fig. 4 *E*). Only amyloid fibrils were observed after seven-day incubation (Fig. 4 *F*), implying that most of the annular protofibrils converted to fibrils. This result was in good agreement with previous reports, which showed that different types of

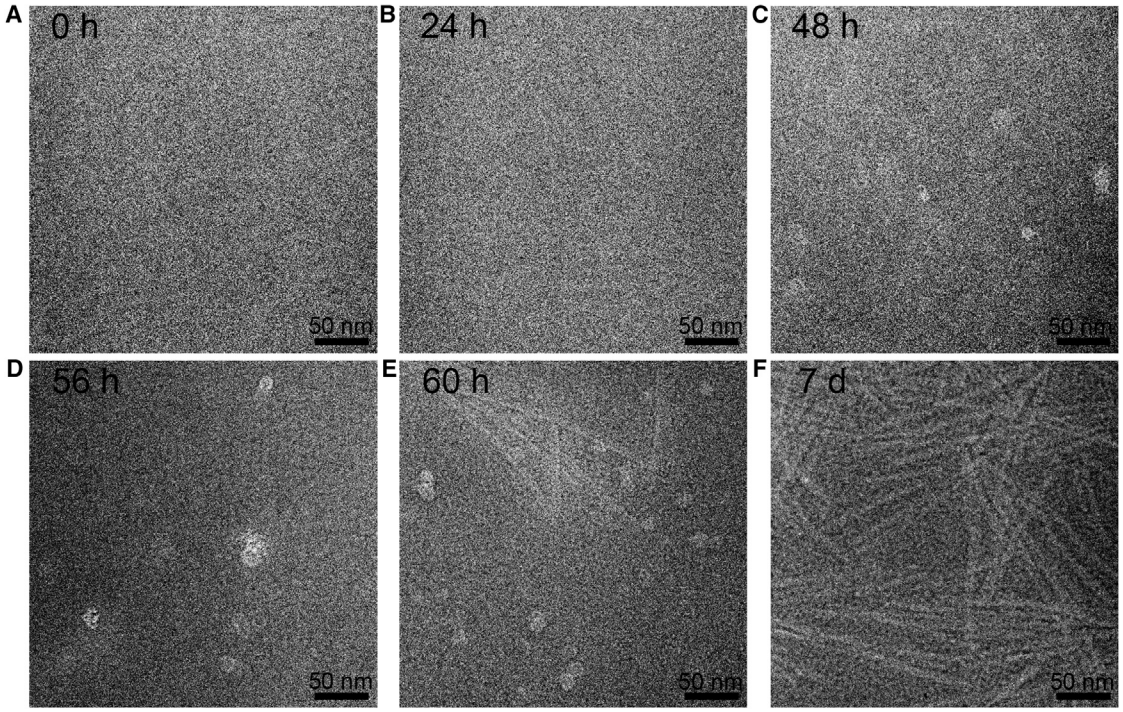

FIGURE 4 Cryo-EM images showing the structures of the aggregates of 400 μM α-synuclein in the presence of 40 μM Cu^{2+} at a series of incubation times (*t*): (*A*) 0 h, (*B*) 24 h, (*C*) 48 h, (*D*) 56 h, (*E*) 60 h, and (*F*) 7 days.

β-sheet rich amyloid protofibrils transiently formed earlier than fibrils and then disappeared along with fibril formation (24,33–35). The aggregation of α-synuclein was in general parallel with the accumulation of β-sheet conformation monitored by ThT fluorescence (Fig. 5).

How did annular protofibrils convert to fibrils? Given the foregoing finding that β-sheet-rich annular protofibrils and protofilaments shared the same width, the conversion from the former to the latter could be achieved simply by ring opening. A few of the particles were captured at the exact transient ring opening moment (Fig. 1, *J* and *K*). Once the rings opened, these structures could already be called protofilaments. Short protofibrils similar to the ones identified in our cryo-EM investigation (and that appeared to consist of paired, parallel protofilaments) were previously observed via negative-stain TEM analysis of A53T α-synuclein and were called tubular protofibrils (17). Our cryo-EM images showed that the annular protofibrils could form long narrow rectangles (the first four images of Fig. 1 *J*) and then transform into two short and parallel protofilaments, which could be easily identified in cryo-NS images (Fig. 1 *K* and see the Supporting Material). This observation suggested that there was lateral interaction between the two parallel subunits resembling the interaction between two filaments. Another clue for elucidating the aggregation mechanism came from Fig. 1 *L*, where annular protofibrils aggregated laterally. These rings were in very close proximity without identifiable gaps, similar to the interaction between two protofilaments within a filament. Through these two types of interactions, the short protofilaments generated from annular protofibrils could easily assemble into short fibrils. The particles in Fig. 6, *A* and *B*, were observed to be short fibrils with two short filaments of $\approx$5.9-nm width each. To show this interesting stage of the aggregation pathway with better contrast, a very large defocus was used in Fig. 6, resulting in an apparent size increase. Upon formation, the short fibrils underwent association (Fig. 6, *A* and *B*) and further connected with one another to form longer fibrils (Fig. 6 *C*), and finally they formed mature fibrils

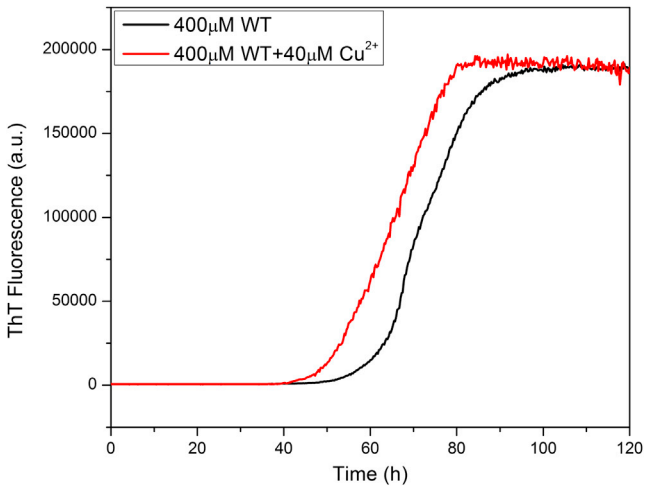

FIGURE 5 The aggregation kinetics of 400 μM α-synuclein in the absence and presence of 40 μM Cu^{2+} monitored with ThT fluorescence.

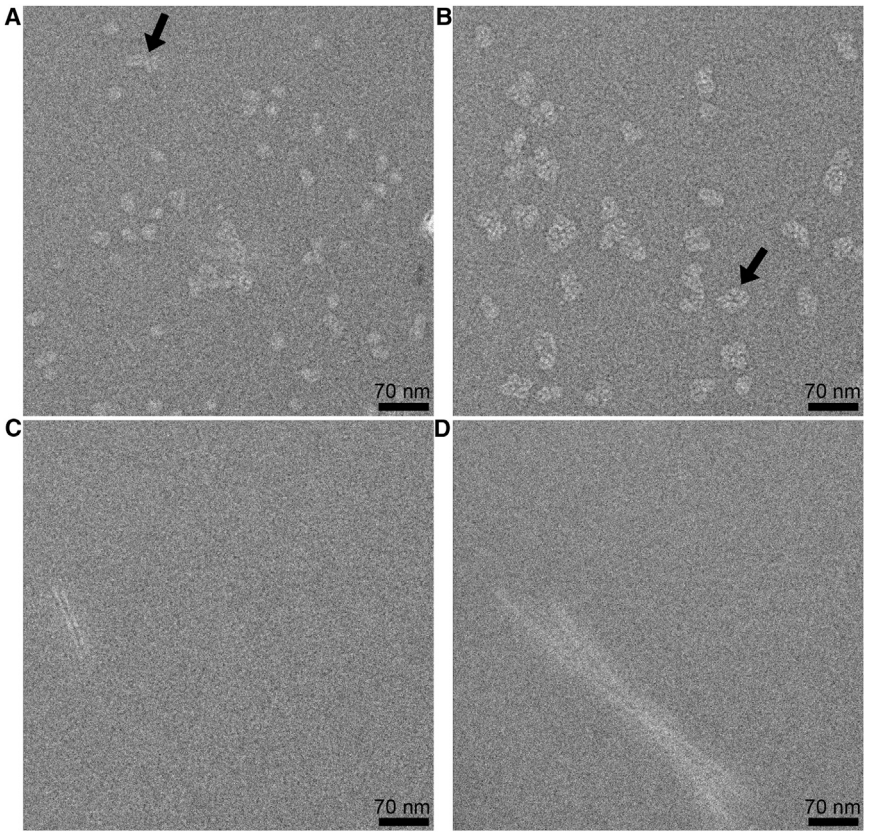

FIGURE 6 Cryo-EM images displaying the aggregation process from protofibrils to fibrils. (*A* and *B*) Images showing presumably transient interactions among protofibrils that could be an early step in the formation of short fibrils. (*Arrows*) Clearest examples. (*C* and *D*) Images of a short fibril (*C*) and mature fibrils (*D*).

(Fig. 6 *D*). The capture of the images showing this aggregation pathway from annular protofibrils to fibrils, in turn supported the perspective that the annular protofibrils might be equivalent to protofilaments within fibrils.

Thus, we propose an α-synuclein aggregation pathway that is mainly based on the capacity of cryo-EM imaging to capture dynamic processes of proteins in solution (Fig. 7). At the beginning, the unstructured monomers convert to a β-sheet conformation and aggregate to small protofibrils, a transition that would be accelerated by pathological factors (7,16). In the next step, the β-sheet rich protofibrils further aggregate into either annular protofibrils or protofilaments by extending the β-sheet structure along the direction perpendicular to β-strands. Generally, the formation of annular protofibrils should not be favored due to the instability of the distorted β-sheet structure. At the same time, the energetically favored protofilaments assemble into mature fibrils via lateral interactions. However, factors such as mutations (17), interactions with bilayer membranes (25), or the exposure to metal ions in

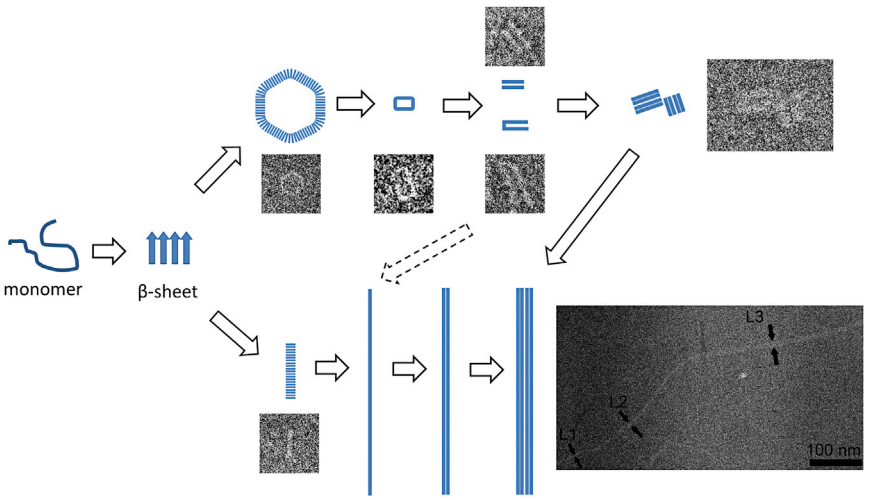

FIGURE 7 The proposed aggregation pathway. Initially, unstructured monomers convert to a β-sheet structure and form small protofibrils. The small protofibrils undergo further assembly to form either annular or linear protofibrils by extending the β-sheet along the direction perpendicular to the β-strands. Linear protofibrils assemble into mature fibrils via lateral interactions (and each linear protofibril can be identified as a protofilament in the mature fibrillar structure). Annular protofibrils convert to fibrils through ring opening followed by interactions among linear protofibrils.

the study described here facilitate the formation of annular protofibrils. Annular protofibrils might convert to fibrils through ring opening and subsequent interactions among linear protofibrils. There was no identifiable difference of the annular structures between the protein samples in the presence and absence of Cu^{2+} (see the Supporting Material), which might just promote the aggregation (Fig. 5) (37,38).

CONCLUSION

In summary, we characterized the protofibril structures in solution with fewer artifacts than by using traditional imaging methods, such as AFM and negative-stain TEM. Hence, we found the correlation of annular protofibrils and fibrils, for the first time to our knowledge, by measuring their true sizes and visualizing the aggregation steps. A better understanding of the aggregation pathway as presented here yields fresh insight into the pathogenesis of amyloid-related diseases, and may provide us the opportunity to develop additional therapeutic strategies to suppress the formation of toxic species in these disorders.

SUPPORTING MATERIAL

Two figures are available at http://www.biophysj.org/biophysj/supplemental/S0006-3495(13)00518-3.

Cryo-EM tests were carried out at the Purdue Biological Electron Microscopy Facility. We thank our colleagues at Markey Center for Structural Biology for discussions.

Supported by National Institutes of Health grants No. K25 NS058395-04 (L.A.S.) and No. R01 NS049221 (J.-C.R.).

REFERENCES

1. de Lau, L. M. L., and M. M. B. Breteler. 2006. Epidemiology of Parkinson's disease. *Lancet Neurol.* 5:525–535.
2. Olanow, C. W., M. D. Stern, and K. Sethi. 2009. The scientific and clinical basis for the treatment of Parkinson disease. *Neurology* 72:S65–S73.
3. Fink, A. L. 2006. The aggregation and fibrillation of α-synuclein. *Acc. Chem. Res.* 39:628–634.
4. Caughey, B., and P. T. Lansbury. 2003. Protofibrils, pores, fibrils, and neurodegeneration: separating the responsible protein aggregates from the innocent bystanders. *Annu. Rev. Neurosci.* 26:267–298.
5. Goldberg, M. S., and P. T. Lansbury, Jr. 2000. Is there a cause-and-effect relationship between α-synuclein fibrillization and Parkinson's disease? *Nat. Cell Biol.* 2:E115–E119.
6. Ross, C. A., and M. A. Poirier. 2004. Protein aggregation and neurodegenerative disease. *Nat. Med.* 10(*Suppl*):S10–S17.
7. Chiti, F., and C. M. Dobson. 2006. Protein misfolding, functional amyloid, and human disease. *Annu. Rev. Biochem.* 75:333–366.
8. Zhang, H., H. Luo, and X. Zhao. 2010. Mechanistic study of self-assembling peptide RADA16-I in formation of nanofibers and hydrogels. *J.Nanotechnol. Eng. Med* 1: 011007–011006.
9. Ruan, L. P., H. Y. Zhang, …, X. Zhao. 2009. Designed amphiphilic peptide forms stable nanoweb, slowly releases encapsulated hydrophobic drug, and accelerates animal hemostasis. *Proc. Natl. Acad. Sci. USA* 106:5105–5110.
10. Bucciantini, M., E. Giannoni, …, M. Stefani. 2002. Inherent toxicity of aggregates implies a common mechanism for protein misfolding diseases. *Nature* 416:507–511.
11. Ye, Z., H. Zhang, …, X. Zhao. 2008. Temperature and pH effects on biophysical and morphological properties of self-assembling peptide RADA16-I. *J. Pept. Sci.* 14:152–162.
12. Kayed, R., E. Head, …, C. G. Glabe. 2003. Common structure of soluble amyloid oligomers implies common mechanism of pathogenesis. *Science* 300:486–489.
13. van Rooijen, B. D., M. M. Claessens, and V. Subramaniam. 2010. Membrane permeabilization by oligomeric α-synuclein: in search of the mechanism. *PLoS ONE* 5:e14292.
14. Conway, K. A., S. J. Lee, …, P. T. Lansbury, Jr. 2000. Acceleration of oligomerization, not fibrillization, is a shared property of both α-synuclein mutations linked to early-onset Parkinson's disease: implications for pathogenesis and therapy. *Proc. Natl. Acad. Sci. USA* 97:571–576.
15. Conway, K. A., J. D. Harper, and P. T. Lansbury, Jr. 2000. Fibrils formed in vitro from α-synuclein and two mutant forms linked to Parkinson's disease are typical amyloid. *Biochemistry* 39:2552–2563.
16. Ding, T. T., S. J. Lee, …, P. T. Lansbury, Jr. 2002. Annular α-synuclein protofibrils are produced when spherical protofibrils are incubated in solution or bound to brain-derived membranes. *Biochemistry* 41:10209–10217.
17. Lashuel, H. A., B. M. Petre, …, P. T. Lansbury, Jr. 2002. Alpha-synuclein, especially the Parkinson's disease-associated mutants, forms pore-like annular and tubular protofibrils. *J. Mol. Biol.* 322:1089–1102.
18. Lashuel, H. A., D. Hartley, …, P. T. Lansbury, Jr. 2002. Neurodegenerative disease: amyloid pores from pathogenic mutations. *Nature* 418:291.
19. Kayed, R., A. Pensalfini, …, C. Glabe. 2009. Annular protofibrils are a structurally and functionally distinct type of amyloid oligomer. *J. Biol. Chem.* 284:4230–4237.
20. Lashuel, H. A., D. M. Hartley, …, P. T. Lansbury, Jr. 2003. Mixtures of wild-type and a pathogenic (E22G) form of Aβ40 in vitro accumulate protofibrils, including amyloid pores. *J. Mol. Biol.* 332:795–808.
21. Lin, H., R. Bhatia, and R. Lal. 2001. Amyloid β protein forms ion channels: implications for Alzheimer's disease pathophysiology. *FASEB J.* 15:2433–2444.
22. Sokolowski, F., A. J. Modler, …, D. Naumann. 2003. Formation of critical oligomers is a key event during conformational transition of recombinant Syrian hamster prion protein. *J. Biol. Chem.* 278:40481–40492.
23. Porat, Y., S. Kolusheva, …, E. Gazit. 2003. The human islet amyloid polypeptide forms transient membrane-active prefibrillar assemblies. *Biochemistry* 42:10971–10977.
24. Lashuel, H. A., and P. T. Lansbury, Jr. 2006. Are amyloid diseases caused by protein aggregates that mimic bacterial pore-forming toxins? *Q. Rev. Biophys.* 39:167–201.
25. Quist, A., I. Doudevski, …, R. Lal. 2005. Amyloid ion channels: a common structural link for protein-misfolding disease. *Proc. Natl. Acad. Sci. USA* 102:10427–10432.
26. Jang, H., F. T. Arce, …, R. Nussinov. 2009. Misfolded amyloid ion channels present mobile β-sheet subunits in contrast to conventional ion channels. *Biophys. J.* 97:3029–3037.
27. Hong, D.-P., A. L. Fink, and V. N. Uversky. 2008. Structural characteristics of α-synuclein oligomers stabilized by the flavonoid baicalein. *J. Mol. Biol.* 383:214–223.
28. Dusa, A., J. Kaylor, …, A. L. Fink. 2006. Characterization of oligomers during α-synuclein aggregation using intrinsic tryptophan fluorescence. *Biochemistry* 45:2752–2760.
29. Kong, J., and S. Yu. 2007. Fourier transform infrared spectroscopic analysis of protein secondary structures. *Acta Biochim. Biophys. Sin. (Shanghai)* 39:549–559.

30. De Carlo, S., and J. R. Harris. 2011. Negative staining and cryo-negative staining of macromolecules and viruses for TEM. *Micron* 42:117–131.

31. Adrian, M., J. Dubochet, …, J. R. Harris. 1998. Cryo-negative staining. *Micron* 29:145–160.

32. Jang, H. B., J. Zheng, …, R. Nussinov. 2008. New structures help the modeling of toxic amyloidβ ion channels. *Trends Biochem. Sci.* 33:91–100.

33. Harper, J. D., C. M. Lieber, and P. T. Lansbury, Jr. 1997. Atomic force microscopic imaging of seeded fibril formation and fibril branching by the Alzheimer's disease amyloid-β protein. *Chem. Biol.* 4:951–959.

34. Lambert, M. P., A. K. Barlow, …, W. L. Klein. 1998. Diffusible, non-fibrillar ligands derived from Aβ1-42 are potent central nervous system neurotoxins. *Proc. Natl. Acad. Sci. USA* 95:6448–6453.

35. Walsh, D. M., A. Lomakin, …, D. B. Teplow. 1997. Amyloid β-protein fibrillogenesis. Detection of a protofibrillar intermediate. *J. Biol. Chem.* 272:22364–22372.

36. Vilar, M., H. T. Chou, …, R. Riek. 2008. The fold of α-synuclein fibrils. *Proc. Natl. Acad. Sci. USA* 105:8637–8642.

37. Rasia, R. M., C. W. Bertoncini, …, C. O. Fernández. 2005. Structural characterization of copper(II) binding to α-synuclein: insights into the bioinorganic chemistry of Parkinson's disease. *Proc. Natl. Acad. Sci. USA* 102:4294–4299.

38. Uversky, V. N., J. Li, and A. L. Fink. 2001. Metal-triggered structural transformations, aggregation, and fibrillation of human α-synuclein. A possible molecular NK between Parkinson's disease and heavy metal exposure. *J. Biol. Chem.* 276:44284–44296.